The metallophilic interaction between cyclometalated complexes: photobiological applications

Zhou, X.

5

Self-assembling cyclopalladated photosensitizers for photodynamic therapy: tumor accumulation and anti-tumor activity in a skin melanoma xenograft

Though small-molecule drugs remain the major form of anticancer chemotherapy, they usually show low tumor accumulation and severe side effects. Nanocarriers are considered to be an appealing strategy to increase drug accumulation in the tumor via the enhanced permeability and retention effect. However, many of these nanocarriers are still limited by low drug-loading capacity and tumor accumulation efficiency. In this work, we designed a molecular photosensitizer self-assembly nanosystem (MoPSAN) based on the supramolecular Pd…Pd interaction between cyclometalated palladium (i.e. cyclopalladated) complexes ***PdL****. On the one hand the drug loading issue of nanocarriers is overcome because each molecule of the self-assembly is a* ***PdL*** *photosensitizer. On the other hand, the photosensitizer is taken up with high efficacy via endocytosis because it is self-assembled into a nanoparticle. As a result, the* ***PdL*** *assembly shows low toxicity in the dark, but upon irradiation with green light it generates massive amount of reactive oxygen species, resulting in effective anticancer effect both in vitro and in a skin melanoma tumor xenografts. Overall, the Pd…Pd interactions stimulate high tumor accumulation efficiency in vivo without jeopardy of the phototoxicity of the photosensitizer, suggesting that this form of supramolecular bonds can be used for the efficient tumor delivery of new nanomedicines.*

This chapter will be submitted as a full paper: X.-Q Zhou, W. Sun*, P. Wang, V. Ramu, S. Jiang, S. Abyar, P. Papadopoulou, Y. Shao, M. A Siegler, F. Buda, A. Kros, S. Bonnet*, *manuscript in preparation.*

5.1 Introduction

Curing cancer is one of the toughest challenges of modern medicine,[1] and chemotherapy remains one of the main tools in oncology: using chemicals to kill cancer cells.[2] However, the small size of many molecular chemotherapy drugs is also responsible for their main disadvantages: chemotherapy suffers from nonspecific delivery, rapid blood clearance, and low accumulation in tumors, which altogether generates severe side effects for cancer patients.[3] To overcome these restrictions, vehicles such as polymer nanoparticles, liposomes, or nanosized inorganic materials, have been developed as drug delivery systems that can be functionalized with molecular chemotherapy drugs.[4-6] In a limited number of systems now clinically applied, such conjugation was shown to decrease the drug's systemic toxicity, protect it from blood/renal clearance, and enhance tumor accumulation *via* the enhanced permeability and retention (EPR) effect.[7, 8] However, many nanocarriers show low drug loading capacity (typically <20%),[9, 10] while the resulting tumor accumulation remains comparatively low: recent studies showed that a median 0.7% only of the administered nanoformulated drug dose ends up in the solid tumor.[10, 11] These shortcomings dramatically restrict the promising clinical potential of nano-sized drug delivery systems.

Recently, a new approach was proposed, called drug self-delivery system (DSDS), which consists in using molecular drugs that self-assemble themselves as nanoparticles and accumulate at the tumor site, without the assistance of any specialized nanocarriers.[12] One main advantage of this approach is the high drug-loading capacity of such systems, as the nanoparticles are solely composed of drug molecules. However, this advantage comes with an obvious disadvantage: keeping a low cytotoxicity to healthy organs is more tricky to achieve, as each nanoparticle brings into a cell many toxic molecules. A solution to this problem is proposed here, and consists of using a light-activatable prodrug, or photosensitizer, as the building block for the DSDS. Such molecules are non-toxic or poorly toxic in the dark, but they can help to generate some highly cytotoxic species by *in vivo* light irradiation of the tumor.[13] This form of prodrugs, called photodynamic therapy (PDT) sensitizers, are currently developed at a high pace in the clinics because of the low side effects experienced by cancer patients.[14-16] At the moment, most clinical PDT photosensitizers work *via* the so-called type II PDT mechanism, which involves the triplet excited state of the photosensitizer (^{3}PS) transferring its energy to triplet ground-state dioxygen ($^3O_2$) to generate cytotoxic singlet dioxygen ($^1O_2$).[17] Ideally, when a sufficient number of PS molecules, enough light, and enough $^3O_2$, are present altogether inside the cancer tissue, very efficient cell death occurs. However, this efficacy can

become dramatically lower in hypoxic regions of the tumors, where $^3O_2$ concentration is low.[18] The photosensitizer used here is of another type: upon light irradiation, its excited triplet state transfers an electron to the surrounding biomolecules, which generates cytotoxic reactive oxygen species (ROS) such as $O_2^{\cdot -}$, $OH^{\cdot}$, and H_2O_2.[19, 20] This mechanism, called PDT type I, also requires a large amount of photosensitizer molecule to be present inside the irradiated tumor tissue, which can be achieved by self-assembly of the PS into nanoparticles. However, it is much less dependent on the concentration of O_2. The results presented here, which combine DSDS and type I PDT photosensitizers to make a MoPSAN, provides a highly antitumor active treatment in a skin melanoma xenograft in mice, notably because high phototoxicity is achieved even in hypoxic cancer cells.

The photosensitizer of interest, **PdL** (Figure 1a), contains a palladium(II) metal center, which is also present in the recent clinically approved PDT sensitizers padeliporfin.[21] In contrast with padeliporfin, however, the bis-cyclometalated palladium compounds presented here self-assembles *via* metallophilic Pd…Pd interactions.[22-24] The M-C bond of cyclometalated complexes compensates for the positive charge of the metal ion, which when combined with the strong π-π stacking of the planar aromatic ligand, allows the metal d_z^2 orbitals of nearby complexes to overlap. This orbital overlap generates the supramolecular metal…metal interactions,[25] which leads not only to a lower HOMO-LUMO gap than in the monomer, but also to self-assembly in aqueous solution.[22, 26] We demonstrate in this work that this new palladium photosensitizer **PdL**, not only self-assembles *via* the Pd…Pd interaction in the blood of mice upon intravenous tail injection, but also that it circulates for hours in the body and leads to tumor accumulation and excellent antitumor effect upon light irradiation 12 h after injection.

5.2 Results

5.2.1 Synthesis and characterization of palladium complex. The cyclometalated palladium complex **PdL** was synthesized by boiling the ligand H_2L and $Pd(OAc)_2$ in acetic acid (Figure 5.1a). The activation of the two C-H bonds of the ligand upon coordination to palladium(II) was unequivocally demonstrated by ESI-MS, ^1H and ^{13}C NMR and X-ray crystal structure determination (Table AIV.1 and Figure 5.1b). The neutral palladium complex crystallized in the centrosymmetric $P2_1/n$ monoclinic space group. The palladium ion is in a square-planar geometry with a dihedral angle N2-C11-C17-N3 of 0.25°, and a low τ value (0.11; this structural parameter characterizes the planar *vs*. tetrahedral geometry of tetracoordinate metal complexes).[27] The structure shows head-to-tail dimers that are stabilized by π-π stacking as demonstrated by the short interplanar distance of 3.4 Å, and by metallophilic interaction, as

shown by the short Pd…Pd distance of 3.518 Å (Figure 5.1b). A DFT model of the dimer confirmed its stability, with a converged Pd…Pd distance of 3.52 Å (Figure 5.1c) that matches well with that observed in the crystal lattice. As shown in the DFT model, the Pd…Pd interaction is derived from the hybridization of both palladium d_{4z}^2 orbitals and π orbitals of the ligand in the HOMO of the dimer. The HOMO-LUMO gap is decreased from −3.543 eV in the monomer to −3.319 eV in the dimer, suggesting a bathochromic shift should be observed in the absorbance spectrum due to the Pd…Pd interaction. TDDFT calculations confirmed this expectation with HOMO-LUMO transitions at 502 nm for the dimer vs. 383 nm for the monomer (Figure 5.1d, Table AIV.2).

When dissolved in DMSO, **PdL** showed a modest absorption band based on ligand-to-ligand charge transfer states (LLCT) in the range 434-540 nm, with a maximum at 481 nm (ε = 3700 M^{-1} cm^{-1}, Figure 1e and Table AIV.3). At concentrations of 10 µM, 100 µM, or 1000 µM in DMSO, the complex showed a constant emission maximum at 564 nm with low phosphorescence quantum yield and short lifetime (Figure 5.1e, φ_p = 0.0008, τ = 0.406 ns, Table AIV.3), characteristic for a monomer **PdL** molecule. However, in a DMSO/H_2O 1:9 volumetric mixture (100 µM), a rapid (<1 min) change of the absorbance spectrum was observed, accompanied by a significant increase of the baseline and the generation of a new absorbance peak at 504 nm, characteristic for the MMLCT states typically from Pd…Pd interaction;[28] the absorption spectra then remained constant for as long as the measurement was continued (30 min, Figure 5.1f). The TEM pictures of this solution showed the self-assembly of **PdL** into nanorods and nanocubes (Figure 1f, insert). Usually, the formation of Pd…Pd supramolecular bonds is accompanied by a long-wavelength emission peak.[28] As shown in Figure 5.1g, an increase of the H_2O content of DMSO (fw = V_{water}/V_{total}) indeed led to a decrease of the monomeric emission peak at 564 nm in pure DMSO (fw = 0.0) and gradual replacement by an emission maximum at 593 nm at fw = 0.5 that evolved into a final band at 610-670 nm (fw = 0.9), concomitant with the formation of a precipitate. In a THF/H_2O solution, similar self-assembly was observed, but with a slower polymerization rate and resulting in different nanostructures as observed with TEM (nanocrystals and nanofibers, Figure AIV.1-2). These results suggest that the structure and size of the nanoparticles derived from **PdL** are highly influenced by the nature of the solvent and the rate of self-assembly.

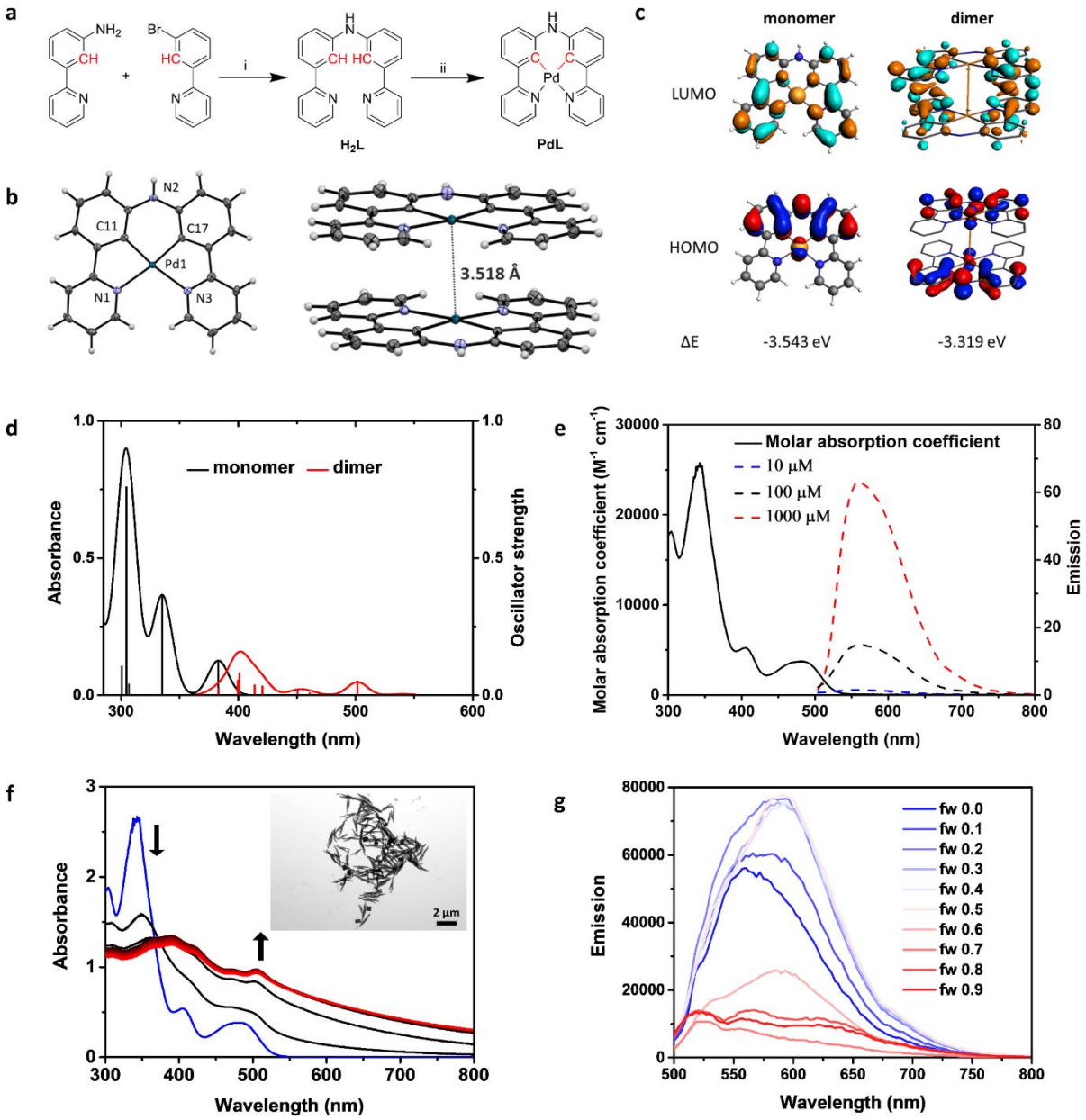

Figure 5.1 *(a) Synthesis of* ***H₂L*** *and* ***PdL*** *((i) Pd(dba)₂, KOt-Bu, BINAP, Toluene, 95 °C, N₂, 72 h, yield 67%; (ii) Pd(OAc)₂, CH₃COOH, 135 °C, 24 h, yield 56%). (b) Displacement ellipsoid plot (50% probability level) of* ***PdL*** *and its stacking structure at 110(2) K. (c) DFT calculation of HOMOs (bottom) and LUMOs (top) orbitals of* ***PdL*** *as a monomer or dimer (calculated Pd…Pd distance 3.52 Å). Occupied orbitals (HOMO) have red and blue lobes, and unoccupied orbitals (LUMO) brown and cyan lobes. Element color code: blue = N, grey = C, brown = Pd, white = H. (d) TDDFT-calculated spectra of* ***PdL*** *as a monomer (red line) or dimer (black line). Level of theory: TDDFT/PBE0/TZP/COSMO (methanol). (e) The absorption spectrum (black solid line) and emission spectra of* ***PdL*** *in pure DMSO solution at different concentrations (blue dash line 10 μM; black dash line 100 μM, red dash line 1000 μM;*

excitation 419 nm). (f) Time evolution of the absorption spectra of DMSO/H_2O solution (100 µM, V/V = 1/9) of ***PdL*** *at 298 K for 30 min (30 s interval, the color of spectra change from black (0 min) to red (30 min); the blue line is the absorbance spectra of* ***PdL*** *(100 µM) in pure DMSO. Inset picture: the TEM images of nanostructures of* ***PdL*** *in DMSO/H_2O solution (100 µM, V/V = 1/9, scale bar 2 µm) (g) Emission spectra of* ***PdL*** *(100 µM) in H_2O/DMSO mixtures with different volumetric ratios (fw = V_{water}/V_{total}).*

5.2.2 Self-assembly of PdL in cell-growing medium. Before evaluating the biological properties of the complex **PdL** in cancer cells, an important but often ignored step consists in determining its self-assembly behavior in cell-growing medium, here Opti-MEM complete containing 2.5 vol% of fetal calf serum (FCS). When the complex (25 µM) was dissolved in medium, aggregation into nanoparticles immediately occurred, as demonstrated by the maximum hydrodynamic diameter of 164 nm determined with dynamic light scattering (DLS, Figure 5.2a). After 30 min, the maximum hydrodynamic diameter of nanoparticles had only slightly shifted (to 190 nm), but the number of particles had increased significantly (Figure AIV.3). The absorption spectrum of **PdL** in medium showed a gradual increase in intensity over 2 h, characteristic for the light-scattering due to self-assembled nanoparticles. After the first 2 h the absorption spectrum remained stable over 24 h, demonstrating the stability of the aggregates for longer time scales (Figure 5.2b). The morphology of the self-assembled nanostructures was then determined using TEM, which showed a stepwise self-assembly process (Figure 5.2c, 50 nm). The structures appeared first as regular hollow nanorods, which gradually lengthened and were surrounded by small nanodots with a much lower thickness-to-length ratio, demonstrating that there might be several nanostructures in medium. According to cryo-EM imaging, the nanofibers had a crystalline structure with a repeating distance of ~1.68 nm, as indicated by fast Fourier transform (Figure 5.2d). On the other hand, fewer nanoparticles were detected in the cryo-EM images than in the TEM images, suggesting that **PdL** might exist both as isolated molecules or small oligomers, and larger nanoaggregates in the medium. In summary, DLS, EM, and UV-vis measurements demonstrated the time-dependent self-assembly of **PdL** into nanorods and nanoparticles in cell-growing medium, which probably form *via* the metallophilic Pd…Pd interactions.

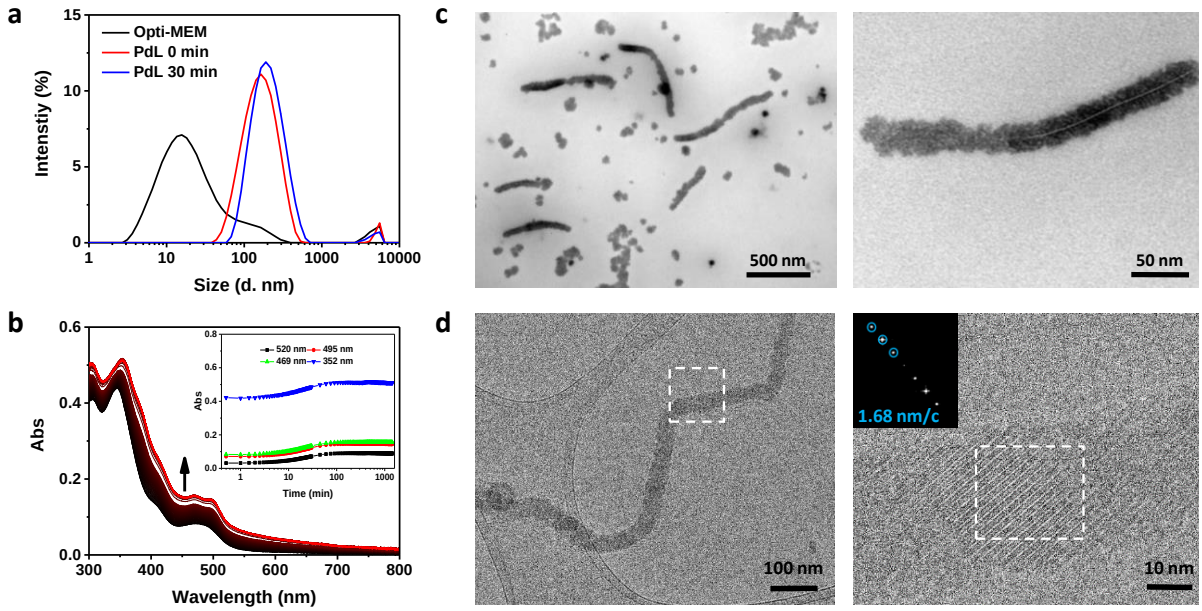

Figure 5.2 *(a) Size distribution of Opti-MEM complete medium, and its* ***PdL*** *(25 µM) solution at 0 min (red line) or 30 min (blue line) according to DLS analysis at room temperature. (b) Observation of absorbance spectra of* ***PdL*** *(25 µM) in Opti-MEM complete medium over 24 h (30 s interval for the first 30 min, 15 min interval for the next 23.5 h). (c, d) TEM images and cryo-EM images of samples prepared from an Opti-MEM complete medium solution of* ***PdL*** *(25 µM) at room temperature.*

5.2.3 Photodynamic properties of PdL in cell-growing medium. The formation of self-assembled nanostructures may influence the photochemical properties of the palladium complex. As mentioned above, PDT may occur either *via* a type I mechanism (electron transfer) or type II (energy transfer) mechanism. Type II photodynamic properties are straightforward to determine *via* direct detection of the near-infrared emission peak of $^1O_2$ at 1270 nm, or *via* indirect detection of $^1O_2$ using chemoselective chemical probes.[29] NIR detection of $^1O_2$ by monomeric **PdL** in MeOD under blue light irradiation (450 nm) showed very low quantum yields for $^1O_2$ generation ($\varphi_\Delta = 0.09$, using **[Ru(bpy)$_3$]Cl$_2$** as standard, $\varphi_\Delta^{ref} = 0.73$, Figure 5.3a, Table AIV.3). To determine the value of φ_Δ of the nano-aggregated **PdL** in Opti-MEM medium, 9,10-anthracenediyl-bis(methylene)-dimalonic acid (ABMDMA) was used as hydrophilic probe for $^1O_2$. In the dark, this dye absorbs light at 378 nm, but in the presence of photogenerated $^1O_2$, it forms an endoperoxide that leads to loss of conjugation and thus a decrease in absorbance at 378 nm. Upon green light irradiation of medium-containing ABMDMA and **PdL** (25 µM**)** , the absorbance of ABMDMA did not decrease significantly (Figure 5.3b), indicating $^1O_2$ generation was negligible (φ_Δ = 0.04; rose bengal used as

standard, φ_Δ = 0.68, Figure AIV.4).[24] Overall, **PdL** was found to be a poor PDT type II sensitizer, both as a monomer and in the polymeric state. By contrast type I PDT sensitizers can be characterized by the generation of superoxide ($O_2^{\bullet-}$) as primary photochemical species, which can further react with many biological substrates to generate other ROS such as $HO^\bullet$ or H_2O_2.[30] When a DMSO or Opti-MEM solution of **PdL** (25 µM) was irradiated with green light (525 nm) in the presence of dihydroethidium (DHE), a chemoselective chemical probe for superoxide, the oxidation product 2-hydroxyethidium was produced efficiently, as shown by its emission at 590-620 nm (Figure 5.3c, **Figure AIV.5**).[31] The results of these experiments suggest that **PdL** is capable of generating superoxide upon green light irradiation, both in the monomeric and in aggregated states, and that this compound is hence essentially a PDT type I photosensitizer that is almost incapable of generating singlet oxygen.

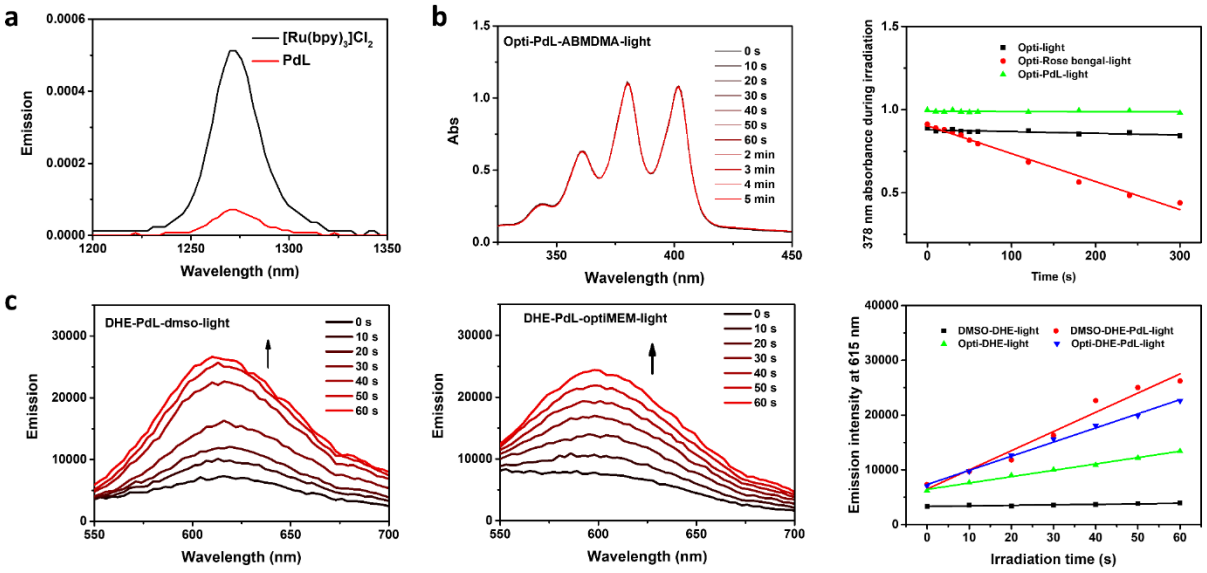

Figure 5.3 *(a) Singlet oxygen emission spectra of $[Ru(bpy)_3]Cl_2$ (black) and* ***PdL*** *(red) in CD_3OD irradiated with blue light (λ_{ex} = 450 nm, 50 mW, 0.4 W/cm^2). (b) The absorbance change of ABMDMA Opti-MEM complete solution (100 µM) in the presence of* ***PdL*** *or rose bengal (25 µM) under green light irradiation (515 nm, 2.0 mW) over 5 min. (c) The emission spectra of a dihydroethidium (DHE) solution (DMSO or Opti-MEM complete) in the presence of* ***PdL*** *(25 µM) under green light irradiation over 60 s.*

5.2.4 Photocytotoxicity, cell death mechanism and *in vivo* tumor inhibition. Considering the significant absorption of 520 nm light by **PdL** (ε = 915 M^{-1} cm^{-1}) and its promising PDT type I properties, its photocytotoxiciy in 2D-monolayers of three different human cancer cells lines (lung carcinoma A549, epidermoid carcinoma A431, melanoma (A375) was evaluated *in vitro* using a reported protocol,[32] both in the dark and under a low dose of green light (520 nm,

13 J/cm^2). **PdL** showed moderate dark cytotoxicity with EC_{50} above 10 µM for the three cancer cell lines under normoxic growing conditions (21% O_2, 37 ˚C). By contrast, after green light irradiation (520 nm, 20 min, 10.9 mW/cm^2, 13 J/cm^2), the complex exhibited high photocytotoxicity with sub-micromolar EC_{50} and a very high photoindex PI = $EC_{50,dark}/EC_{50,light}$ of 72 (Figure 5.4a, **Figure AIV.6** and Table 1). Interestingly, in A375 cells growing in hypoxic conditions (1% O_2) the EC_{50} of **PdL** also decreased dramatically upon the same dose of green light irradiation, *i.e.* from 15.9 µM in the dark to 0.49 µM after activation with green light, thus demonstrating outstanding PDT efficacy of this complex even at low dioxygen concentrations. The cell death mode resulting from the PDT treatment with **PdL** was determined *via* Annexin V/Propidium iodide double staining experiments using flow cytometry either 2 h, 4 h, or 24 h after irradiation (Figure 5.4b and Figure AIV.7). Clearly, **PdL** (0.5 and 2 µM) showed no or limited cell death in dark conditions. In the irradiated group, no toxicity was observed after 2 h, but after 4 h and 24 h, the number of apoptotic and necrotic cells had increased significantly, suggesting that **PdL** started to induce cancer cell death 4 h after irradiation *via* both cell death mechanisms.

3D multicellular tumor spheroid models provide a more accurate biological evaluation not only of compound toxicity but also of the physical penetration of light, drugs, and nanoparticle-based delivery systems.[33] The photocytotoxicity of **PdL** in A549 and A375 spheroids was hence determined using a CellTiter-Glo end-point viability assay in 96-well round-bottom Corning spheroid plates. In the dark, **PdL** was nearly non-toxic to A549 spheroids ($EC_{50,\ normoxic}$ > 25 µM), while moderate toxicity was observed for A375 tumor spheroids ($EC_{50,\ normoxic}$ = 9.19 µM, $EC_{50,\ hypoxic}$ = 14.3 µM). However, after green light irradiation, **PdL** showed nearly 100-folds increase in cytotoxicity, leading to submicromolar EC_{50} values (around 0.20 µM), accompanied by the visible collapse of the spheroid cores and dramatic shrinking of the spheroid diameters (Figure 5.4c, AIV.8 and Table 1). A further Hoechst 33342/Propidium iodide double-staining experiment was carried out to compare the morphology and health status of A375 spheroids treated with **PdL** (2 µM) and either kept in the dark or irradiated with green light (520 nm, 32 min, 6.9 mW/cm^2, 13 J/cm^2). Hoechst 33342 results in staining the nucleus of all cells with blue fluorescence, while propidium iodide only stains dead cells with red fluorescence. As shown in Figure 5.4c, in the dark only limited propidium iodide emission was detected, which demonstrated that the tumor spheroid was essentially intact. In the green-light irradiated group, the red fluorescence of propidium iodide significantly increased, accompanied by the obvious collapse of the spheroid core, confirming the excellent PDT effect of **PdL** in 3D tumor

spheroids. Remarkably, the complex is non-toxic in the dark but highly phototoxic to cancer cells at 1 µM both in a 2D and 3D environment, and both in presence of high or low O_2 concentrations, suggesting that further *in vivo* testing in mice xenografts may be tried to assess the delivery and antitumor efficacy of this compound in a medicinally more relevant cancer model.

Melanoma is one of the most aggressive skin cancer types, which is attributed to cause 80% of deaths related to skin cancer worldwide, though it only represents 4% of diagnosed skin cancer patients.[34] Among the various methods used to treat melanoma, PDT represents one of the most promising alternatives due to the excellent accessibility of skin for light irradiation, and significant skin penetration of visible light.[35] However, A375 melanoma was also reported to be particularly prone to developing a hypoxic tumor microenvironment, which quenches PDT type II photosensitizers, but may represent no limitation to type I photosensitizers.[36] The *in vivo* PDT effect of **PdL** was hence evaluated on human A375 tumor xenografts in nude mice. After tail intravenous injection with **PdL** (2.1 µmol/kg, 0.9 mg/kg, 420 µM, 100 µL saline), the mice showed constant body weight (Figure 5.4d) compared with the control groups, which is a sign of low systemic toxicity. This result was confirmed by H&E staining analysis that demonstrated that at this dose **PdL** was not toxic to important organs such as the heart, liver, lung, and kidneys (Figure AIV.9). In the dark group, **PdL** showed a moderate tumor growth inhibition, matching with its modest dark cytotoxicity to cancer cells *in vitro*; after green light irradiation (520 nm, 100 mW/cm^2, 10 min, 60 J/cm^2), tumor growth was significantly inhibited by **PdL** over 20 days (Figure 5.4e). H&E staining of the irradiated tumors revealed that the tumor tissues were dramatically damaged in the **PdL+light** group, while the other groups did not show any remarkable effect (Figure 5.4f); the TUNEL staining, an assay to evaluate the number of apoptotic cells in tissues, also demonstrated the dramatic decrease and damage of cancer cells in the irradiated tumor (Figure 5.4f), while the control groups showed no effect. These experiments demonstrated that **PdL** not only shows excellent antitumor efficacy in the A375 melanoma mice model, but that this compound also shows very low cytotoxicity to healthy organs, highlighting the high potential of **PdL** for anticancer PDT application.

Table 1. *Half-maximal effective concentration (EC_{50} in µM) of* ***PdL*** *for A549, A5431 and A375 cancer cells in normoxic, hypoxic or 3D-normoxic and 3D-hypoxic spheroids conditions under dark or green light irradiation. 95% confidence interval (CI in µM) and photoindex (PI = $EC_{50,\ dark}/EC_{50,\ light}$) are also indicated.*

Cell line		**EC_{50} Values (µM)**							
	Condition	2D Normoxic		2D Hypoxic		3D Normoxic		3D Hypoxic	
A549	dark	12	+1 -1	17.2	+1.5 -1.3	>25			
	light	0.18	+0.02 -0.02	0.47	+0.04 -0.03	0.26	+0.01 -0.01	N.D	
	PI	68		37		>96			
A431	dark	20.3	+1.1 -1.1	15.6	+1.7 -1.6				
	light	0.45	+0.06 -0.05	0.9	+0.1 -0.1	N.D		N.D	
	PI	45		17					
A375	dark	12.3	+1.3 -1.4	15.9	+1.6 -1.4	9.19	+2.1 -1.8	14.3	+4.9 -2.7
	light	0.17	+0.01 -0.01	0.49	+0.09 -0.07	0.17	+0.01 -0.02	0.20	+0.01 -0.01
	PI	72		32		54		72	

Irradiation condition: normoxic 520 nm, 20 min, 10.9 mW/cm^2, 13 J/cm^2 ; hypoxic 520 nm, 30 min, 7.22 mW/cm^2, 13 J/cm^2; 3D-normoxic 520 nm, 32 min, 6.90 mW/cm^2, 13 J/cm^2; 3D-hypoxic 520 nm, 55 min, 3.99 mW/cm^2, 13.2 J/cm^2. Data is the mean over three independent experiments. N.D means not determined.

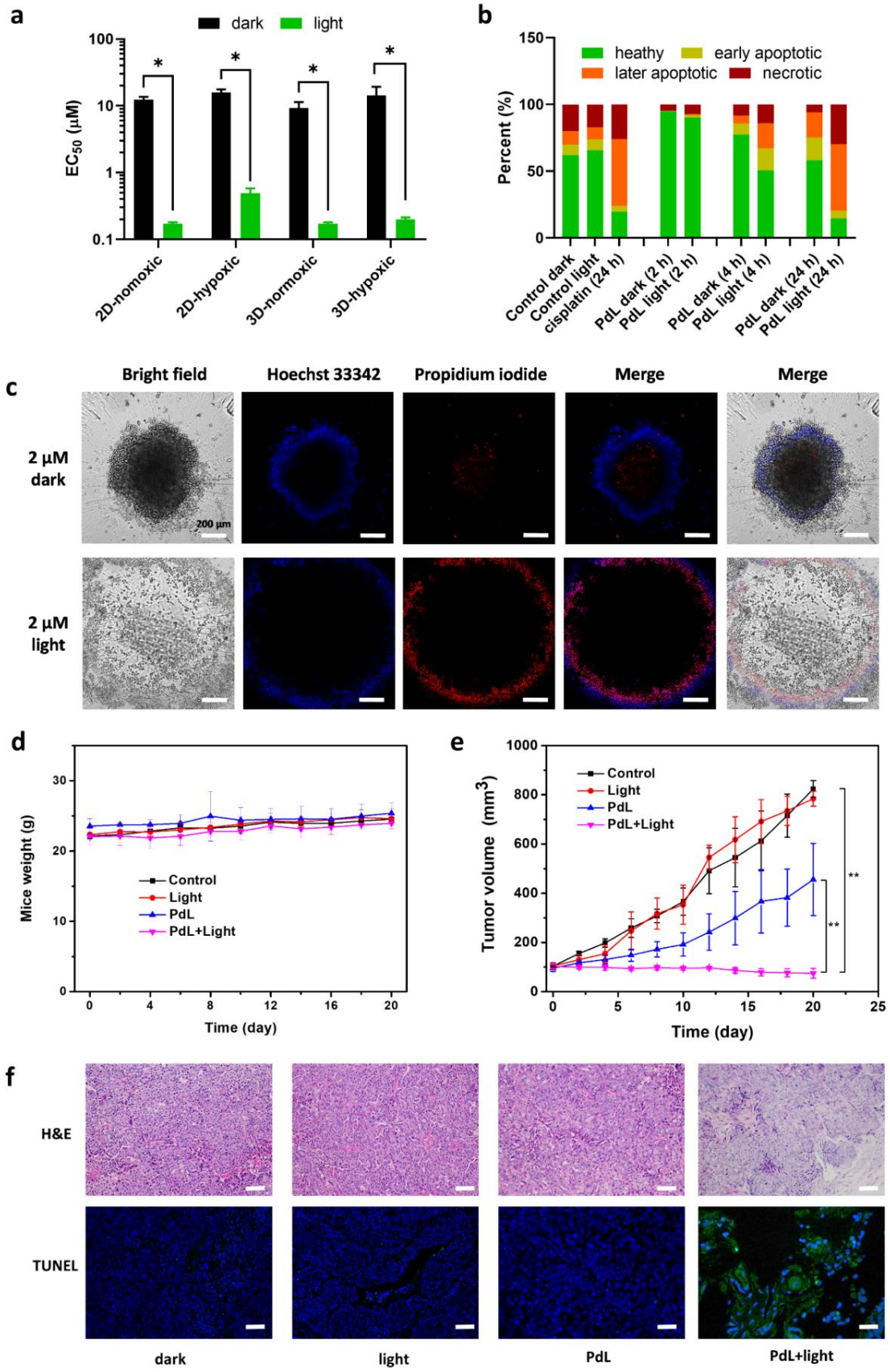

Figure 5.4 *(a) EC_{50} values of* ***PdL*** *to A375 2D-monolayer and 3D-spheroid cancer cells incubated, either in the dark or upon green light irradiation (13 J/cm^2), and in normoxic or*

hypoxic conditions; statistical significance was set to p < 0.05 (*). (b) Flow cytometry quantification of healthy, early apoptotic, later apoptotic and necrotic A375 cells after treatment with ***PdL*** *(2 µM) in the dark or with green light irradiation in a time gradient (2 h, 4 h, 24 h). Cisplatin (7.5 µM, 24 h) is used as positive control (c) Confocal images of 3D-normoxic A375 spheroids (scale bar 200 nm) in the dark or green light irradiation, with Hoechst 33342/Propidium iodide double staining after treated with* ***PdL*** *(2 µM) for 72 h. (d) Time evolution of the mice weight 20 days post-treatment. (e) A375 tumor growth inhibition in different mice groups treated by tail intravenous injection; N=3, statistical significance was set to p < 0.01 (**). Light irradiation condition: 520 nm, 100 mW/cm^2, 10 min, 60 J/cm^2. Dose: 2.1 µmol/kg, 0.9 mg/kg, 420 µM, 100 µL saline. (f) H&E and TUNEL staining assay to tumor slices of mice in different groups at day 5.*

5.2.5 Uptake and biodistribution of PdL nanoparticles *in vitro* and *in vivo*. The low systemic dark toxicity and high antitumor PDT efficacy of **PdL** stimulated us to check the drug uptake *in vitro* and *in vivo*. ICP-MS was hence used to determine the Pd content in A375 cells. The Pd content in A375 cell monolayers was 29 ng Pd/million cells 2 h after treatment with **PdL** (2 µM, Figure 5.5a); after 24 h treatment, the Pd content was increased about 6-fold to 172 ng per million cells, with an uptake efficiency up to 34% (uptake efficiency (%) = total Pd mass in cells/total Pd mass in working solution×100%). When A375 cells were incubated with **PdL** (5 µM) for 2 h at 4 °C, the cellular uptake was significantly reduced to 19 ng/million cells, compared to the 37 °C control (44 ng/million cells, Figure 5.5b). This result suggests that 57% of the cellular uptake of **PdL** is energy-dependent, while 43% of internalization takes place *via* passive diffusion or energy-independent channels. A possible interpretation of this combined active/passive uptake is that **PdL** probably is present in cell medium both as nanoparticles and isolated molecules, which are taken up by different mechanisms. Active transport was definitively demonstrated by the lower Pd content found in cells co-incubated with **PdL** and either NaN_3, pitstop, or wortmannin, while nocodazole and dynasore did not show any inhibition of the **PdL** uptake (Figure 5.5b). These data showed that active internalization probably occurred *via* clathrin-mediated endocytosis and micropinocytosis, while phagocytosis and dynamin-dependent endocytosis can be excluded. Overall, it appears that **PdL** mainly passes through the cell membrane *via* both energy-independent transport and endocytosis, which is consistent with the hypothesis of **PdL** being taken up both as mononuclear molecules, and as nanoparticles.

An essential question at this stage is to understand whether the nanoparticles formed by **PdL** *in vitro* would also form in living mice and may explain the antitumor selectivity observed in mice tumor xenografts. The presence and morphology of these nanostructures were tested in living mice. First, a blood sample was taken 5 min after intravenous tail injection of **PdL** (2.1 μmol/kg, 0.9 mg/kg, 420 μM, 100 μL saline). As shown in Figure AIV.10, the blood sample showed roughly spherical high-contrast nanoparticles with an average size of 181±75 nm, which were not found in the blood samples of Pd-free mice, and matched very well with the nanoparticle average diameter observed for **PdL** *in vitro*. This important result suggested that **PdL** can keep self-assembling as nanoparticles in the blood. In a second step, 12 h after tail injection with **PdL** the A375 tumor of mice xenografts was sectioned using an ultramicrotome and the slices were imaged with EM. The EM images (Figure 5.5c, 1 and 0.5 μm scale, pointed out by red arrows) showed dark nano-sized spots in the cytoplasm of the cancer cells with an average diameter at 260±75 nm, slightly larger than the diameter of nanoparticles in the cell medium and blood. These dark spots are characteristic for heavy-metal containing nanoparticles, and altogether strongly suggest that **PdL** accumulated at least partly as nanoparticles in the cytoplasm of tumor cells. The larger nanoparticle size in the tumor indicated that upon accumulating in the tumor tissue and entering the cells, the self-assembly of **PdL** present in the blood may be labile enough to rearrange into other shapes and sizes, which highlights the supramolecular nature of the Pd…Pd interaction. Interestingly, in the large scale EM image of the tumor slice, several long nanofibers were detected as well (width around 150 nm, Figure 5.5c, 10 μm scale), which might be attributed to **PdL.** These fibers are reminiscent of the nanofibers found when **PdL** was dissolved in THF/H_2O mixtures, which were characterized by a 100 nm width **(**Figure AIV.1). Overall, the presence of nanoparticles both in the blood and in the tumor tissue of mice treated with **PdL** is a proof-of-concept that self-assembly of the Pd sensitizer in blood leads to delivery of the prodrug to the tumor, which lies at the core of MoPSAN.

In order to assess whether this tumor delivery was selective or not, the biodistribution of **PdL** was determined in mice xenografts. Several hours (2, 6, 12, 20, 24 h) after intravenous tail injection of **PdL** (2.1 μmol/kg, 0.9 mg/kg, 420 μM, 100 μL saline), the Pd content of several healthy organs as well as that of the tumor, were determined with ICP-OES. As shown in Figure 5.5d, the complex showed low accumulation (below 0.27 μg/g tissue) in the heart, kidney, and lung, while the liver showed significantly higher accumulation (above 1.0 μg/per gram tissue), as expected considering its role in detoxification and metabolism of exogenous substances.

Noticeably, the accumulation level of **PdL** in the liver gradually decreased in time, from 3.5 µg/g tissue 2 h after injection to 1.0 µg/g tissue 24 h after injection. Meanwhile, the tumor tissue showed an increased Pd accumulation from 0.17 to 0.87 µg/g tissue during the first 12 h, and further decreased to 0.17 µg/per gram tissue at 20 h and 24 h. These data suggest that **PdL** nanostructures either withstand initial rapid accumulation in the liver, to relocate at the tumor site, or that they accumulate in parallel in the tumor site and liver, but at different rates. In any case, they show a metabolic cycle around 12-20 h. Besides, **PdL** shows a comparatively extraordinary efficient tumor accumulation efficacy, that culminates to 10.2 %ID/g [percent injected dose per gram of tissue (%ID/g) = (Pd content of tumor/Pd content of injection solution)×100%/mass of measured organs] at 12 h post-injection (Figure 5.5e). This exceptional drug delivery efficacy, which can probably be attributed to the EPR effect, confirms the high *in vivo* potential of the DSDS principle, here applied to a PDT type I photosensitizer. Critically, the high drug accumulation in the liver is not an issue because of the much lower toxicity of **PdL** when it is not irradiated by light. The specific application of drug self-delivery system for the photosensitizer **PdL** makes this MoPSAN approach very advantageous, compared to traditional nanoconjugates chemotherapy.

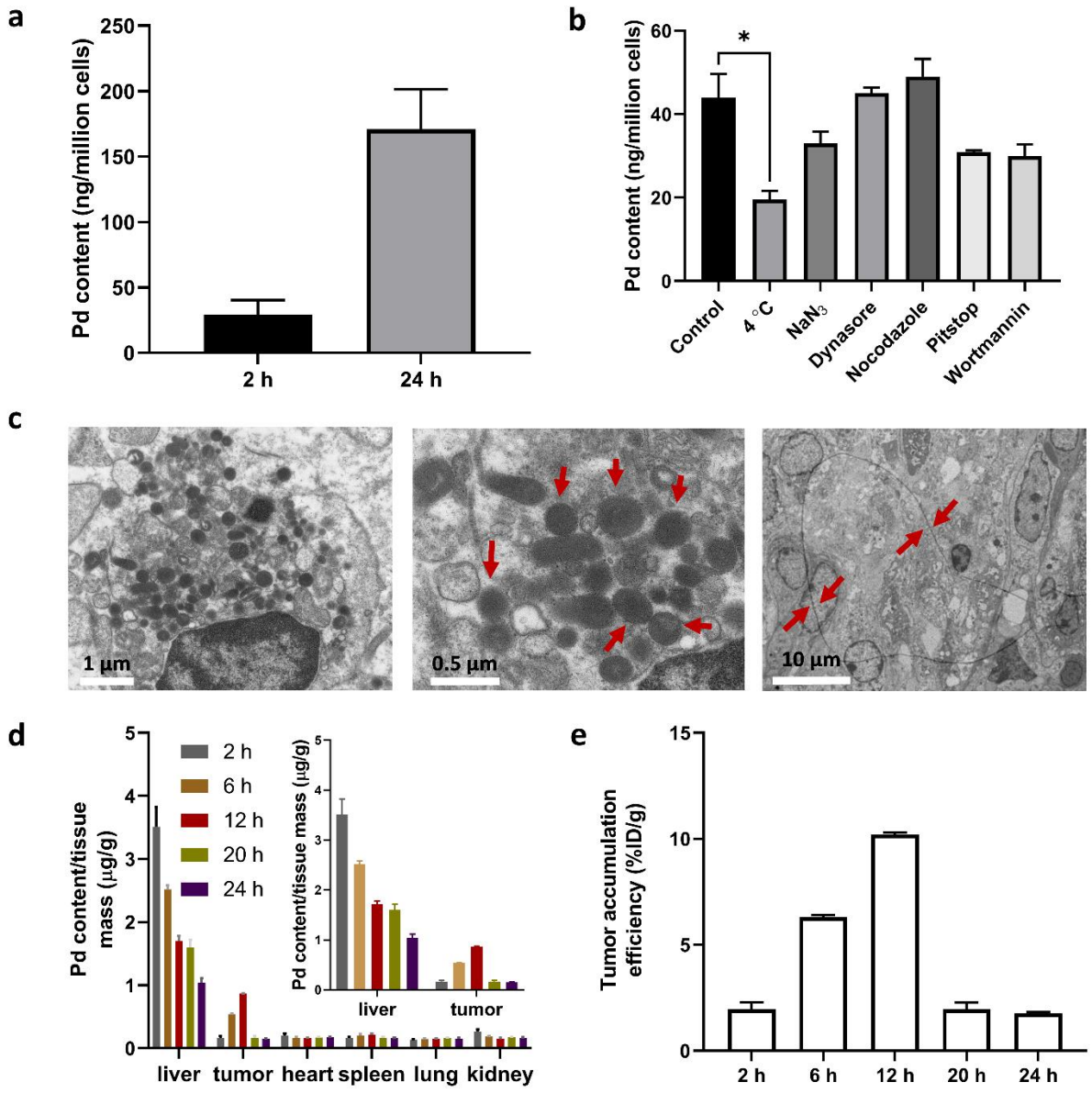

Figure 5.5 *The Pd content (ICP-MS) of A375 skin melanoma cell monolayers treated with* ***PdL*** *(a) at 2 μM after 2 or 24 h, and (b) at 5 μM after 2 h in combination with different uptake inhibition pretreatment. (c) EM images at a different magnification of slices of A375 tumor xenografts in mice 12 h after intravenous tail injection of* ***PdL.*** *Nanoparticles and nanofibers are indicated by red arrows. (d) Biodistribution of palladium (ICP-MS) in different organs of mice at different time points after intravenous tail injection of* ***PdL****. (e) Tumor palladium accumulation efficiency in mice at different time points after intravenous tail injection by* ***PdL****. %ID/g = (Pd content of tumor/Pd content of injection solution)×100%/mass of measured organs). In vivo injection conditions: 420 μM, 100 μL saline.*

5.3 Discussion

PDT offers an alternative to chemotherapy, with the potential to inhibit tumor proliferation while minimizing side-effects.[17] In principle, the physical selectivity offered by light irradiation of the tumor tissue ensures antitumor selectivity. However, photosensitizer molecules taken up in healthy tissues lead to undesired photosensitivity (*e.g.* skin) for the patient, a typical side-effect of PDT with Photofrin for example.[37] It is hence essential that the photosensitizer is delivered with high efficacy to the tumor tissue. Many reports have demonstrated that nanoconjugates enable to increase the tumor accumulation of molecular drugs, including PDT photosensitizers.[38, 39] However, a recent report has revealed the low average drug-loading capacity (typical 20 wt%) and tumor accumulation efficacy (mediumn 0.7 %ID) of classical drug delivery nanosystems,[10] indicating the urgency to develop new nanosystems to solve the drug-loading and nanoparticle delivery problem. In this work, the drug-loading issue of the nanoparticle is overcome by the self-assembly of photosensitizer **PdL**. This self-assembly provides long circulation times (12-20 h) and a drug accumulation in the tumor tissue that is much higher (up to 10.2 %ID/g) than for traditional nanoconjugates, giving a strong indication that Pd…Pd interactions can be used to deliver anticancer (pro)drugs to tumors with high efficacy.

The other challenges relevant to PDT compounds are hypoxia and light penetration, which severely limit their photodynamic effect. Several innovative solutions have been proposed to solve the hypoxia problem. Nanoparticle-based drug delivery systems that evolve O_2, for example, can improve the local O_2 concentration in hypoxic tumor tissues before irradiation of the sensitizer, which recovers the photodynamic activity of photosensitizers observed in normoxic regions.[40, 41] Others have combined photosensitizers and chemotherapy *via* hypoxia-activated linkers.[42] Still, the complexity and low reproducibility of multicomponent nanoparticles endanger the clinical application of these systems.[43] By contrast, MoPSAN relies on a simple PDT type I molecular sensitizer, **PdL**, that can be reproducibly synthesized and self-assemble spontaneously in the blood into well-characterized nanoparticles. In this work, we choose A375 skin melanoma cancer models to test the PDT effect of MoPSAN because of the suitable skin penetration of visible light [44] and the highly hypoxic microenvironment of skin melanoma tumor.[45] Besides, melanoma is the most dangerous form of skin cancer and resistant to several PDT agents, probably due to the optical interference of highly-pigmented melanin.[35] Nevertheless, the *in vitro* and *in vivo* results demonstrate the significant green light-activated PDT effect of **PdL** even in presence of low dioxygen concentrations, suggesting the MoPSAN

may be a feasible strategy to overcome PDT resistance in skin melanoma. One remaining question is whether MoPSAN would stimulate T-cell activation and generate antitumor immune memory and systemic response after PDT treatment, which could not be investigated here to the immunoincompetent character of the mice used.[46]

5.4 Conclusion

The new MoPSAN strategy, which consists of a molecular photosensitizer that self-assembles into long-circulating nanoparticles in blood, generates a very powerful PDT agent. As an isolated molecule, this palladium complex shows significant $O_2^{\bullet-}$ generation upon green light irradiation, making it a good PDT type I sensitizer. In addition, the strong supramolecular Pd…Pd interaction lets this complex self-assembly in biological medium such as blood, where the molecule is present as soluble nanoparticles. This spontaneous aggregation provokes, within 12 h, drug accumulation in the tumor *via* the EPR effect, and cellular uptake by a combination of passive and active transport. Importantly, these palladium nanoaggregates conserve the PDT type I properties of the monomer. This observation makes **PdL** to be a fundamentally different sensitizer compared with many porphyrin-based ones, which typically lose their photodynamic properties upon aggregation. With these results in hand, we conclude that the metallophilic Pd…Pd interaction has a high potential 1) to build supramolecular nanocarriers with improved tumor accumulation *via* the EPR effect, and 2) to generate PDT photosensitizers that conserve their phototoxic properties under hypoxia. With both properties combined, the MoPSAN demonstrate promising anti-tumor properties, here in skin melanoma xenograft models.

5.5 Experimental section

The DFT calculation, photophysical spectra, TEM, Cryo-EM, cell culture, photocytotoxicity, cell uptake and apoptosis experiments were carried out according to the description in chapter 3 and 4.

5.5.1 Synthesis and NMR characterization of ligands and metal complexes.

H_2L, (bis(3-(pyridin-2-yl)phenyl)amine)

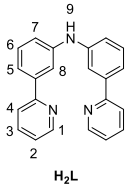

H_2L

A mixture of 2-(3-bromophenyl)pyridine (329 mg, 1.41 mmol), $Pd(dba)_2$ (81 mg, 0.14 mmol), racemic BINAP (106 mg, 0.17 mmol) and KO*t*-Bu (1574 mg, 14 mmol) was partially dissolved in dry toluene (28 mL) under N_2 atmosphere. The mixture was stirred for 10 min, then 3-(2-Pyridyl)aniline (230 mg, 1.35 mmol) was added, followed by heating the reaction mixture to 95 °C. After 3 days of stirring, the brown mixture

was cooled down. Demi water (75.0 mL) was added and the mixture was stirred for 1 h. The H_2O layer was separated from the toluene layer. Extracted the H_2O layer with EtOAc (100 mL) for three times and combined the toluene and EtOAc layers, followed by rotary evaporation of the solvents. The crude product was purified by silica chromatography using pentane-EtOAc mixtures (2:1, R_f = 0.3) as eluent, to afford 290 mg of the target compound **H_2L^1** (yield: 0.90 mmol, 67%). **ESI-MS** (cation): m/z calcd 324.2 ($C_{22}H_{17}N_3$ + H^+), found 324.7. **^{1}H NMR** (300 MHz, DMSO-*d_6*): δ 8.65 (dt, *J* = 4.7, 1.4 Hz, 2H, H^1), 8.49 (s, 1H, H^9), 7.97 – 7.81 (m, 6H, H^5, H^8, H^3), 7.53 (dt, *J* = 7.8, 1.3 Hz, 2H, H^4), 7.42 – 7.30 (m, 4H, H^6, H^2), 7.20 (dd, *J* = 7.8, 2.3 Hz, 2H, H^7). **^{13}C-APT NMR** (75 MHz, DMSO-*d_6*): δ 156.1, 149.5, 143.8, 139.7, 129.6, 122.6, 120.2, 120.2, 118.1, 117.4, 115.1.

PdL

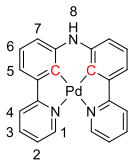

PdL

A mixture of **H_2L** (90 mg, 0.28 mmol) and $Pd(OAc)_2$ (63 mg, 0.28 mmol) in a glacial acetic acid was refluxed for 24 h at 135 °C under N_2 atmosphere to give a yellowish green solution. Then the solvent was rotary evaporated. The crude product obtained was purified by silica chromatography using DCM/MeOH mixtures (v/v = 100:1.5, R_f =0.3) as eluent, to afford 67 mg of target complex **PdL** (yield: 0.15 mmol, 56%). **ESI-MS** (cation): m/z calcd 428.0379 ($C_{22}H_{15}N_3Pd$ + H^+), found 428.0374. **^{1}H NMR** (300 MHz, DMSO-*d_6*) δ 9.20 (s, 1H, H^8), 8.94 (d, J = 5.4 Hz, 2H, H^1), 8.20 (d, J = 8.1 Hz, 2H, H^4), 8.10 – 8.00 (m, 2H, H^3), 7.49 (ddd, J = 7.1, 5.5, 1.3 Hz, 2H, H^2), 7.46 – 7.37 (m, 2H, H^5), 7.14 (t, J = 7.6 Hz, 2H, H^6), 7.00 (dd, J = 7.9, 1.1 Hz, 2H, H^7). **^{13}C** NMR (75 MHz, DMSO-*d_6*) δ 163.77, 148.75, 146.55, 139.56, 138.71, 137.87, 124.64, 122.74, 119.50, 115.14, 114.52. **Elemental analysis** calcd for **PdL**: C 61.77, H 3.53, N 9.82; found: C 61.93, H 3.64, N 9.60.

5.5.2 *In vivo* tumor inhibition experiments. Female BALB/c mice with 3 weeks old were originally purchased from Vital River Laboratory Animal Center (Beijing, China). The mice were kept under specific pathogen-free conditions with free access to standard food and water for 2 weeks, to let the mice weight around 20 g. This study was conducted following the Guide for the Care and Use of Laboratory Animals published by the US National Institutes of Health (8th edition, 2011). All protocols for animal studies conformed to the Guide for the Care and Use of Laboratory Animals. All animal experiments were performed under guidelines approved by the ethics committee of Peking University. The tumor model was established by inoculating 5×10^7 of A375 melanoma cells suspended in 100 μL of PBS at the right flank region of each mouse, to obtain mouse A375 melanoma implant. 3 weeks later, the tumor volumes were

around 100 mm^3. Tumor volume (V) can be calculated by formula $V = L/2 \times W^2$ after measuring the tumor length (L) and width (W).[47] The mice were then randomly divided into 4 groups (vehicle control, 520 nm light, **PdL**, **PdL**+520 nm light groups, each group 4 mice). The mice were treated through tail intravenous injection with saline for vehicle control and 520 nm light groups, or **PdL** (2.1 μmol/kg, 0.9 mg/kg, 420 μM, 100 μL saline) for **PdL** and **PdL**+520 nm light groups. After 12 h injection, 520 nm irradiation (100 mW/cm^2, 5 min) was then carried out twice, with an interval of 5 min for the light groups. Thus, the total light dose for each treatment was 100 mW/cm^2, 10 min, 60 J/cm^2. These treatment and irradiation steps were replicated at day 0, day 7 and day 14, respectively. On day 5, one mouse in each group was sacrificed and the tumor was taken up and fixed with paraformaldehyde (10% v/v), then sectioned into slices and analyzed *via* H&E or TUNEL protocols, to evaluate the tumor cell damage and apoptosis conditions. The tumor volume and body weight of left mice (N=3) were measured and recorded and the average tumor volume and body weight were calculated over 20 days. At last, the mice were sacrificed, and the healthy organs were taken up, fixed with paraformaldehyde (10% v/v), then sectioned into slices and analyzed *via* H&E protocol, to determine side effect of **PdL** after treatment.

5.5.3 Mice blood EM imaging experiments. The tumor-bearing mouse was treated with **PdL** (2.1 μmol/kg, 0.9 mg/kg, 420 μM, 100 μL saline) through intravenous tail injection. After 5 min, 1 mL of blood was taken up from the eye socket and diluted to 5 mL by PBS. After centrifugation (1500 rpm, 10 min), the supernatant was collected, and the left part was washed by PBS (5 mL) and centrifuged (1500 rpm, 10 min) again twice more, to obtain the supernatant PBS solution. These PBS solutions were then combined and centrifuged at a speed of 10000 rpm for 10 min. After removing the supernatant, 200 uL PBS were added and mixed well. Then the solutions were transferred to the TEM grids. For the preparation of TEM samples, a drop (15 μL) of the solution was added to the grids (formvar/carbon 200 Mesh, copper) and kept for 2 min, then the excess liquid on the grid was removed by filter paper, and dried for 2 h for TEM measurement. The TEM measurements were carried out in vacuum conditions (HITACHI H-7650).

5.5.4 Mice tumor EM imaging experiments. One tumor-bearing mouse was treated with **PdL** (2.1 μmol/kg, 0.9 mg/kg, 420 μM, 100 μL saline) through intravenous tail injection. After 12 h, the mouse was sacrificed, the tumor tissue was collected and then fixed by a biological TEM fixation solution (Wuhan Servicebio). After that, the tumor tissue was split into small pieces with volume around 1 mm^3, and fixed again using 1 % osmic acid PB solution for 2 h, following

with dehydration by ethanol (v/v = 30 %, 50 %,70 %, 80 %, 95 %,100 %, each group 20 min) and acetone for two times (15 min). The prepared samples were then treated with acetone/epon-812 embedding medium in the ratio 1:1 for 2 h, 1:2 for 12 h, and pure epon-812 solution for another 5 h at 37 ˚C. After that, the tissue-containing embedding medium was filled in the embedding mold for 24 h at 37 ˚C, and another 60 °C for 48 h. The obtained tissue-containing resins were then sectioned into slices with thickness around 60-80 nm via ultramicrotome (Leica EM UC7), and moved to the copper grid (150 mesh). The obtained grids were stained by 2 % uranyl acetate ethanol solution for 8 min, and 2.6 % lead citrate solution for another 8 min. After that, the grids were dried at room temperature and observed using JEOL JEM2100 TEM (Japan).

5.5.5 Pd distribution determination on mice organs. The mice were treated with **PdL** (2.1 μmol/kg, 0.9 mg/kg, 420 μM, 100 μL saline) through intravenous tail injection. Then, the mice were sacrificed at 2 h, 6 h, 12 h, or 20 h, or 24 h, and their heart, liver, spleen, kidney, lung, and tumor were taken. Then, around 1 g of each organ were lysed overnight in a mixture solution of 65% HNO_3 (5 mL) and 30% H_2O_2 (2 mL) at 100 °C. Afterward, each sample was evaporated and another 5 mL HNO_3 solution (2%) was added. The Pd content in each organ or tumor was detected *via* ICP-OES (JY-Horiba ICP-OES Ultima 2).

5.6 References

1. R. L. Siegel, K. D. Miller and A. Jemal, *CA Cancer J. Clin.*, 2020, **70**, 7-30.
2. B. A. Chabner and T. G. Roberts, *Nat. Rev. Cancer*, 2005, **5**, 65-72.
3. Z. G. Chen, *Trends Mol. Med.*, 2010, **16**, 594-602.
4. M. Zeinali, S. Abbaspour-Ravasjani, M. Ghorbani, A. Babazadeh, T. Soltanfam, A. C. Santos, H. Hamishehkar and M. R. Hamblin, *Drug Discov. Today*, 2020, **25**, 1416-1430.
5. J. Nam, S. Son, K. S. Park, W. Zou, L. D. Shea and J. J. Moon, *Nat. Rev. Mater.*, 2019, **4**, 398-414.
6. S. Pottanam Chali and B. J. Ravoo, *Angew. Chem. Int. Ed.*, 2020, **59**, 2962-2972.
7. M. Chidambaram, R. Manavalan and K. Kathiresan, *J. Pharm. Pharm. Sci.*, 2011, **14**, 67-77.
8. V. P. Chauhan, T. Stylianopoulos, J. D. Martin, Z. Popovic, O. Chen, W. S. Kamoun, M. G. Bawendi, D. Fukumura and R. K. Jain, *Nat. Nanotechnol.*, 2012, **7**, 383-388.
9. R. B. Greenwald, Y. H. Choe, J. McGuire and C. D. Conover, *Adv. Drug Deliv. Rev.*, 2003, **55**, 217-250.
10. S. Wilhelm, A. J. Tavares, Q. Dai, S. Ohta, J. Audet, H. F. Dvorak and W. C. Chan, *Nat. Rev. Mater.*, 2016, **1**, 1-12.
11. Q. Dai, S. Wilhelm, D. Ding, A. M. Syed, S. Sindhwani, Y. Zhang, Y. Y. Chen, P. MacMillan and W. C. W. Chan, *ACS Nano*, 2018, **12**, 8423-8435.
12. S. Y. Qin, A. Q. Zhang, S. X. Cheng, L. Rong and X. Z. Zhang, *Biomaterials*, 2017, **112**, 234-247.
13. S. B. Brown, E. A. Brown and I. Walker, *Lancet Oncol.*, 2004, **5**, 497-508.
14. H. Huang, S. Banerjee, K. Qiu, P. Zhang, O. Blacque, T. Malcomson, M. J. Paterson, G. J. Clarkson, M. Staniforth, V. G. Stavros, G. Gasser, H. Chao and P. J. Sadler, *Nat. Chem.*, 2019, **11**, 1041-1048.
15. J. Karges, S. Kuang, F. Maschietto, O. Blacque, I. Ciofini, H. Chao and G. Gasser, *Nat. Commun.*, 2020, **11**, 3262.
16. N. Kotagiri, G. P. Sudlow, W. J. Akers and S. Achilefu, *Nat. Nanotechnol.*, 2015, **10**, 370-379.

17. S. A. McFarland, A. Mandel, R. Dumoulin-White and G. Gasser, *Curr. Opin. Chem. Biol.*, 2020, **56**, 23-27.
18. L. Larue, B. Myrzakhmetov, A. Ben-Mihoub, A. Moussaron, N. Thomas, P. Arnoux, F. Baros, R. Vanderesse, S. Acherar and C. Frochot, *Pharmaceuticals*, 2019, **12**.
19. A. P. Castano, T. N. Demidova and M. R. Hamblin, *Photodiagnosis Photodyn. Ther.*, 2004, **1**, 279-293.
20. M. S. Baptista, J. Cadet, P. Di Mascio, A. A. Ghogare, A. Greer, M. R. Hamblin, C. Lorente, S. C. Nunez, M. S. Ribeiro, A. H. Thomas, M. Vignoni and T. M. Yoshimura, *Photochem. Photobiol.*, 2017, **93**, 912-919.
21. A.-R. Azzouzi, S. Vincendeau, E. Barret, A. Cicco, F. Kleinclauss, H. G. van der Poel, C. G. Stief, J. Rassweiler, G. Salomon, E. Solsona, A. Alcaraz, T. T. Tammela, D. J. Rosario, F. Gomez-Veiga, G. Ahlgren, F. Benzaghou, B. Gaillac, B. Amzal, F. M. J. Debruyne, G. Fromont, C. Gratzke and M. Emberton, *Lancet Oncol.*, 2017, **18**, 181-191.
22. A. Aliprandi, M. Mauro and L. De Cola, *Nat. Chem.*, 2016, **8**, 10-15.
23. D. A. K. Vezzu, J. C. Deaton, J. S. Jones, L. Bartolotti, C. F. Harris, A. P. Marchett, M. Kondakova, R. D. Pike, and S. Huo, *Inorg. Chem.*, 2010, **49**, 5107-5119.
24. X. Q. Zhou, M. Xiao, V. Ramu, J. Hilgendorf, X. Li, P. Papadopoulou, M. A. Siegler, A. Kros, W. Sun and S. Bonnet, *J. Am. Chem. Soc.*, 2020, **142**, 10383-10399.
25. M. Mauro, A. Aliprandi, D. Septiadi, N. S. Kehr and L. De Cola, *Chem. Soc. Rev.*, 2014, **43**, 4144-4166.
26. Q. Wan, W. P. To, C. Yang and C. M. Che, *Angew. Chem. Int. Ed.*, 2018, **57**, 3089-3093.
27. X. Q. Zhou, A. Busemann, M. S. Meijer, M. A. Siegler and S. Bonnet, *Chem. Commun.*, 2019, **55**, 4695-4698.
28. C. Zou, J. Lin, S. Suo, M. Xie, X. Chang and W. Lu, *Chem. Commun.*, 2018, **54**, 5319-5322.
29. J. Karges, F. Heinemann, M. Jakubaszek, F. Maschietto, C. Subecz, M. Dotou, R. Vinck, O. Blacque, M. Tharaud, B. Goud, E. Viñuelas Zahínos, B. Spingler, I. Ciofini and G. Gasser, *J. Am. Chem. Soc.*, 2020, **142**, 6578-6587.
30. S. Monro, K. L. Colon, H. Yin, J. Roque, 3rd, P. Konda, S. Gujar, R. P. Thummel, L. Lilge, C. G. Cameron and S. A. McFarland, *Chem. Rev.*, 2019, **119**, 797-828.
31. H. M. Peshavariya, G. J. Dusting and S. Selemidis, *Free Radic. Res.*, 2007, **41**, 699-712.
32. V. Vichai and K. Kirtikara, *Nat. Protoc.*, 2006, **1**, 1112-1116.
33. J. Friedrich, C. Seidel, R. Ebner and L. A. Kunz-Schughart, *Nat. Protoc.*, 2009, **4**, 309-324.
34. S. Kuphal and A. Bosserhoff, *J. Pathol.*, 2009, **219**, 400-409.
35. Y. Y. Huang, D. Vecchio, P. Avci, R. Yin, M. Garcia-Diaz and M. R. Hamblin, *Biol. Chem.*, 2013, **394**, 239-250.
36. M. P. O'Connell, K. Marchbank, M. R. Webster, A. A. Valiga, A. Kaur, A. Vultur, L. Li, M. Herlyn, J. Villanueva, Q. Liu, X. Yin, S. Widura, J. Nelson, N. Ruiz, T. C. Camilli, F. E. Indig, K. T. Flaherty, J. A. Wargo, D. T. Frederick, Z. A. Cooper, S. Nair, R. K. Amaravadi, L. M. Schuchter, G. C. Karakousis, W. Xu, X. Xu and A. T. Weeraratna, *Cancer Discov.*, 2013, **3**, 1378-1393.
37. S. I. Moriwaki, J. Misawa, Y. Yoshinari, I. Yamada, M. Takigawa and Y. Tokura, *Photodermatol. Photoimmunol. Photomed.*, 2001, **17**, 241-243.
38. L. Salvioni, M. A. Rizzuto, J. A. Bertolini, L. Pandolfi, M. Colombo and D. Prosperi, *Cancers*, 2019, **11**.
39. Z. Yu, P. Zhou, W. Pan, N. Li and B. Tang, *Nat. Commun.*, 2018, **9**, 5044.
40. J. Kim, H. R. Cho, H. Jeon, D. Kim, C. Song, N. Lee, S. H. Choi and T. Hyeon, *J. Am. Chem. Soc.*, 2017, **139**, 10992-10995.
41. W. Fan, W. Bu, B. Shen, Q. He, Z. Cui, Y. Liu, X. Zheng, K. Zhao and J. Shi, *Adv. Mater.*, 2015, **27**, 4155-4161.
42. D. Cui, J. Huang, X. Zhen, J. Li, Y. Jiang and K. Pu, *Angew. Chem. Int. Ed.*, 2019, **58**, 5920-5924.
43. D. R. Baer, *Front. Chem.*, 2018, **6**, 145.
44. C. Ash, M. Dubec, K. Donne and T. Bashford, *Lasers Med. Sci.*, 2017, **32**, 1909-1918.
45. O. Distler, J. H. Distler, A. Scheid, T. Acker, A. Hirth, J. Rethage, B. A. Michel, R. E. Gay, U. Muller-Ladner, M. Matucci-Cerinic, K. H. Plate, M. Gassmann and S. Gay, *Circ. Res.*, 2004, **95**, 109-116.
46. J. M. Dabrowski and L. G. Arnaut, *Photochem. Photobiol. Sci.*, 2015, **14**, 1765-1780.
47. W. Sun, J. Fan, S. Wang, Y. Kang, J. Du and X. Peng, *ACS Appl. Mater. Interfaces*, 2018, **10**, 7832-7840.